

# Numerical Simulated Concept and Mechanical Proof of Concept for a Transmission OCT (tOCT)

Andreas Drauschke<sup>1</sup>, Katharina Dettelbacher<sup>1</sup>, Michaela Kienberger<sup>1</sup>, Sarah Nagl<sup>1</sup>  
and Christian Milz<sup>2</sup>

<sup>1</sup>Department Life Science Engineering, UAS Technikum Wien, Höchstädtplatz 6, Vienna, Austria

<sup>2</sup> Faculty of Physics, TU Wien, Wiedner Hauptstraße 8–10, Vienna, Austria

Keywords: Medical Imaging, Biomedical Optics, OCT.

Abstract: Optical coherence tomography is a very powerful tool in imaging methods, but its practical use is limited due to the shallow scan depth. A concept draft of a transmission OCT is presented, which eliminates the greatest limitation of the OCT – the small penetration depth. The functional principle, based on the basic structure of a Mach–Zehnder interferometer, is developed in a numerical simulation in OpticStudio. The numerical setup includes beam expander and beam compressor systems to maximize the contrast generated in the interference pattern and the design of an A–scan to realize a depth scan. As the result, the numerical simulation of the complete setup is presented and the concept is then demonstrated in a simplified mechanical setup without an A–scan.

## 1 INTRODUCTION

Imaging processes play a central role in medical diagnostics and in assisted surgical interventions (Bushberg et al., 2012; Webster et al., 2000; Drexler and Fujimoto, 2015). Among other things, this is due to the fact that modern medical imaging processes have made enormous progress in recent years and not only have the quality of existing diagnostic processes and assistance systems been optimized, but a large number of new areas of applications has been established as well (Samei and Peck, 2019). Some of the most frequently used imaging procedures are listed in table 1. The methods are compared with one another with regard to three important characteristics: the depth of penetration in tissue, the achievable lateral and depth resolution and the distinction between invasive and non-invasive techniques. In addition, some typical applications of the respective processes are listed.

Optical coherence tomography is mostly used as a non-invasive optical imaging technique with which near-surface tissue structures can be imaged in three dimensions or as two-dimensional cross-sections in high resolution (Fercher et al., 2003a; Brezinski, 2006; Drexler and Fujimoto, 2015; Fujimoto and Swanson, 2016). OCT is most commonly used in ophthalmology, for example to make diagnostic scans of the retina.

The OCT is based on the realization of a Michelson interferometer. The backscattered light is used in the sample arm. The penetration depth is limited to a maximum of 3 mm (Drexler and Fujimoto, 2015), due to the physical principle of using backscattered light, which considerably limits the use of the OCT. An interesting aspect of OCT is that the lateral and axial resolution can be influenced independently of one another. The generated images usually have a high resolution and are only exceeded in terms of lateral resolution by microscopy techniques, which lack axial penetration depth.

In order to overcome the essential limitation of OCT, the evaluation of the forward-scattered light appears to be effective. Since no light is scattered antiparallel to the illumination in such a setup in the sample arm, the basic structure of a Michelson interferometer can no longer be used. It makes sense to use a Mach–Zehnder interferometer (Demtröder, 2009) as an alternative interferometric setup for the forward-scattered light, in which the interference pattern is not generated by interference with reflected or backscattered light, but in the transmitted or forward-scattered light. Since this corresponds to an OCT setup in transmission, it is referred to as a transmission OCT (tOCT).

The assignment of an interference pattern to a specific point in the analyzed tissue is more com-

Table 1: Comparison of different imaging techniques in terms of resolution, scan depth and invasive or non-invasive intervention and applications. Computed tomography (CT), positron emission tomography (PET), single-photon emission computed tomography (SPECT), magnetic resonance imaging (MRI), ultrasound (US), optical coherence tomography (OCT) and various microscopy techniques (Bushberg et al., 2012; Webster et al., 2000; Vo-Dinh, 2003; Drexler and Fujimoto, 2015; Hoppert, 2003; Fujimoto and Swanson, 2016; Guggenheim et al., 2017; Rathod et al., 2015; Schützenberger et al., 2019).

imaging technique	invasive/non-invasive	resolution [axial/lateral]	scanning depth of penetration	examples of application
CT	invasive/ionizing radiation	0.5 mm/0.6 mm	whole body	Imaging of the brain, heart, lung, abdomen, tumors, complicated bone fractures, angiography
PET	invasive/ionizing radiation	5 mm/5 mm	whole body	Oncology, neuroimaging, cardiology
SPECT	invasive/ionizing radiation	10 mm/10 mm	whole body	Myocardial scintigraphy, skeletal scintigraphy, brain perfusion scintigraphy, oncology
MRI	non-invasive	0.9 mm/0.9 mm	whole body	Neuroimaging, cardiovascular imaging, musculoskeletal imaging, angiography, liver and gastrointestinal imaging
MRI	invasive/contrast agent	0.9 mm/0.9 mm	whole body	Detection of inflammations or tumors or the higher-contrast imaging of vessels
US	non-invasive	10 $\mu$ m/300 $\mu$ m	20 cm	Imaging of muscles, tendons, and most internal organs
OCT	non-invasive	1–15 $\mu$ m/5 $\mu$ m	2–3 mm	Ophthalmology, dermatology (early cancer diagnosis)
OCT	invasive/in combination with endoscopic methods	1–15 $\mu$ m/5 $\mu$ m	2–3 mm	Imaging of blood vessels, heart, intestines, bladder, cancer diagnosis (early stage), follow-up treatment and diagnosis of a heart attack
various microscopic techniques	non-invasive	–/50 nm (superresolution) 200 nm (classical)	0 mm	Imaging on surfaces or transparent tissue, ophthalmology, imaging in cell cultures
various microscopic techniques	invasive/in combination with endoscopic methods	–/50 nm (superresolution) 200 nm (classical)	0 mm	Imaging on surfaces of blood vessels, heart, bladder

plicated in forward-scattered light, since unscattered light would be directly superimposed on scattered light. Therefore, the scattered light offset with regard to the illumination path will have to be analyzed.

In the presented work the design of a tOCT is realized as a numerical concept and its fundamental capability for generating an interference pattern is demonstrated. The basic suitability for the realization of an A-scan is demonstrated in the numerical simulation.

The suitability of a Mach-Zehnder interferometer is then shown in a simplified setup that does not include an A-scan. For this purpose, an interference pattern is generated as a result of the superposition of the reference beam with forward-scattered light in the sample arm.

The proofs of concepts, both the numerical simulation and the practical implementation in the demonstrator, prove the basic suitability of the setup for the implementation of a transmission OCT.

## 2 MATERIALS & METHODS

### 2.1 Physical Principles

The conceptual transmission OCT is intended to analyze the depth information of a tissue by means of the evaluation of forward-scattered light in contrast to classic OCT, in which backscattered light is analyzed. The greater scan depth of the tOCT is explained by the larger forward scatter in relation to the back scatter of the light. Due to the complexity of biological tissue, an analytical description of the overall physical situation is not possible. The theory of Mie scattering (Mie, 1908; Born and Wolf, 2005; Bhandari et al., 2011) can be used to estimate the ratio of the forward to backscattering. For this it is assumed that the light is scattered by approximately spherical particles, as shown in figure 1.

This is a very rough approximation because, on the one hand, the particles in biological tissue are usually not spherical and, on the other hand, the distance between the scattering particles is small enough that there is a direct interaction between the scattering par-

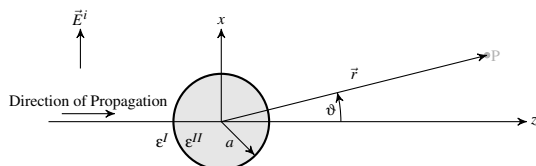


Figure 1: Basic geometry for describing the scattering of light on spherical particles (Mie scattering) according to Born & Wolf (Born and Wolf, 2005).

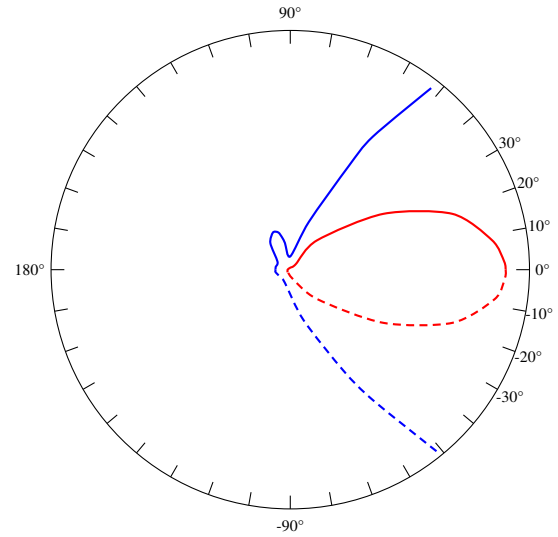


Figure 2: Scattering by a spherical water droplet with drop radius of  $a = 260$  nm (red line),  $a = 2600$  nm (blue line) with  $n = 1.33 + i10^{-8}$  illuminated by visible light of wavelength  $\lambda = 550$  nm according to figure 4.9 from Bohren & Huffman (Bohren and Huffman, 1983). Linear scale; solid line: perpendicular polarization direction, dashed line: parallel polarization direction.

ticles. However, the estimate shows at least the rough tendency of the expected scatter distribution.

An analysis of the scattered light distribution takes place in the graphic evaluation of the scatter amplitude as a function of the scatter angle. The associated graphic representation is referred to as a polar diagram as shown in figure 2. The result of the Mie theory is that the forward scattering tends to increase with increasing particle size, while at the same time the scattering amplitude of the backward scattering tends to decrease (Bohren and Huffman, 1983). In backscattering, a local maximum of the amplitude can be found at a scattering angle of 180 deg under certain physical conditions. With sufficiently large particles (far from the Rayleigh domain) one always finds a local maximum in forward scattering, the amplitude of which is significantly greater than that of backward scattering. For this reason, light in forward scattering can generally achieve a higher scan depth than in backward scattering with the same absorption. Since these effects are wavelength-dependent, it will be necessary to determine the optimal wavelength for use in the tOCT.

It is assumed here that light, which is scattered only once, emerges from the sample at a certain angle. As a further approximation, the tissue is initially assumed to be a plane-parallel plate as shown in figure 3, so that the geometric relationships for analyzing the scattered light are further simplified.

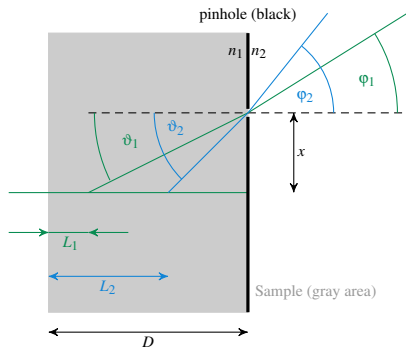


Figure 3: Sketch for determining the correlation between penetration depth  $L_n$  and transmission angle  $\varphi_n$ .

Both approximations of the plane-parallel arrangement of the boundary surfaces most likely lead to inaccuracies in the signal at large exit angles, while the approximation of the single scattering most likely leads to inaccuracies in the interference pattern for small scattering angles. In practice, both errors will become noticeable as a decreasing contrast of the interference pattern.

By applying the two approximations, a direct correlation between the exit angle of a beam – offsetted to the illuminating beam – and the depth-localization of the scattering location in the tissue can be derived. An A-scan is therefore converted into an exit angle spectrum. The physical conditions are shown in figure 3. Simple geometrical considerations and the application of the law of refraction at the point of beam exit lead to

$$\varphi_n(L_n) = \sin^{-1} \left( \frac{n_1}{n_2} \sqrt{\frac{x^2}{(D - L_n)^2 + x^2}} \right). \quad (1)$$

An amplitude scan (A-scan) describes the basic form of a depth-scan (Fercher et al., 2003b). This term most commonly appears in the field of ultrasonography but, can be applied to other imaging modalities such as OCT and tOCT in the same manner. For the A-scan the magnitude of the signals, which in reflective setups results from echoes returning from a different depth within the tissue, are displayed as a function

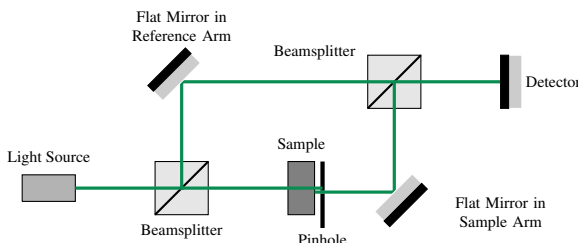


Figure 4: General setup of the Mach-Zehnder interferometer without A-scan for the realization of a transmission OCT according to Demtröder (Demtröder, 2009).

of distance (Dance et al., 2014).

In the case of tOCT the more general explanation of the A-scan, as a scan along one axis, is needed. However, the analysis of this A-scan differs from that of reflective setups. While imaging tools such as ultrasonography detect the depth information along one axis at a single detector element, the scan is transformed to a detection along several detector elements for tOCT. This is due to the exiting angle being a function of penetration depth thus transferring depth-information to an axis perpendicular to the incident light.

The basis of the conceptual transmission OCT is a Mach-Zehnder interferometer, as shown in figure 4. The unmodified reference arm of the classical Mach-Zehnder interferometer is adopted, while a pinhole is added in the sample arm next to the test sample. With the help of this pinhole, those rays scattered in the test sample can be selected. Since the scattered rays do not run parallel to the illuminating beam, it is to be expected in this setup that the structure only leads to an interference pattern on the receiver for small exit angles. Therefore, for the proof of concept, the pinhole was only shifted by approximately 1 mm so that the illuminating beam was just faded out, but the scattered beam was still propagated almost parallel to the illuminating beam. Due to the small angle, it is to be expected that a slightly distorted interference pattern will be generated.

Since only nearly parallel rays generate an interference pattern after passing through the second beam splitter cube, the generated angle spectrum must be transformed into a bundle of parallel rays. The simplest method of parallelizing rays emitted from a point is to place a concave mirror or converging lens at the distance of the focal length to the exit point. To avoid aberrations, a parabolic mirror or an aspherical lens must be used. We decided to use an aspherical lens for the construction in the full setup as shown in figure 5. The A-Scan is thereby converted into a bundle of parallel light beams, with different distances between the light beams and the unscattered beam representing different depths of scattering in the tissue.

## 2.2 Numerical Design

The concept of the transmission OCT was examined in a numerical simulation. For this purpose, in addition to a simulation of the scattering properties of the samples, an aspherical lens was integrated into the structure that implements the A-scan. Additionally, a beam expander was set into the reference arm so that all the beams generated of the A-scan overlap with

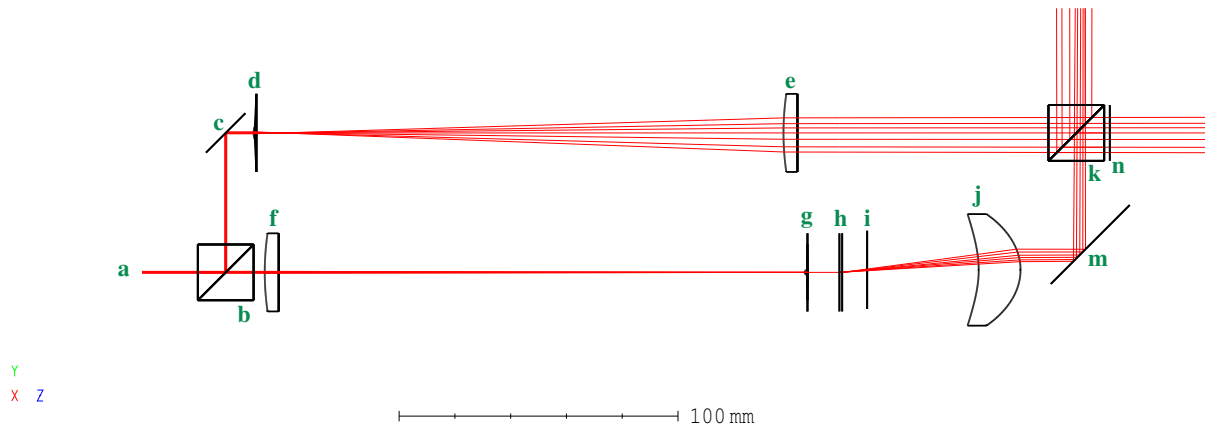


Figure 5: Numerical simulation of the Mach-Zehnder interferometer including A-Scan using OpticStudio (ZEMAX LLC, 2020). Some parameters of the components are listed in table 2: (a) coherent light source, (b) & (k) beam splitter cube, (c) & (m) redirection mirror, (d) & (e) lenses for simulation of a beam expander, (f) & (g) lenses for simulation of a beam compressor, (h) test sample, (i) pinhole, (j) collimator lens, and (n) possible detector position.

beams in the reference arm and thus generate a corresponding interference pattern. In order to determine the location of the scattering in the sample more precisely and to achieve a higher intensity of the beams in the sample arm, a beam compressor was integrated into the sample arm.

The scatter in the sample can in principle be simulated in different ways. In the analyses, Lambert scattering on the one hand and Gauss scattering on the other hand were examined. It turned out that the simulation with a Gauss scattering produced more realistic results, so that in the end a simulation with a Gauss scattering with  $\sigma = 0.2$  was carried out.

Two scattering angles were simulated: 3.52 deg and 6.15 deg. A radius of 1.5 mm was assumed for the reference sphere. Both scattering angles generate an interference pattern on the detector. The interference pattern were determined using a Jones calculus.

The two angles were then collimated with an aspherical lens. This special aspherical lens was designed for this in order to minimize aberrations. In practice, the lens will have to be adapted to the conditions of manufacture. However, the minimization of the aberrations will also be essential for a lens in a real setup in order to keep the reduction of the contrast in the interference pattern as low as possible.

Since only two relatively small angles were simulated, no total internal reflection occurred at the interface between the tissue and the surrounding air. Total internal reflection is to be expected for larger scattering angles and limits the scanning depth of the method. The total internal reflection could be reduced or even completely prevented by adding a transparent contact gel with an adapted refractive index and a field lens at the level of the pinhole at the interface between

tissue and surrounding air.

## 2.3 Proof of Concept in Mechanical Setup

In order to provide the proof of concept by means of a generated interference pattern, the simplified mechanical setup from figure 4 was implemented. In addition, only a very small offset of the pinhole by 1 mm could be implemented. If the offset was greater, the intensity of the scattered beam dropped significantly, so that the interference pattern could no longer be generated. This effect was reinforced by the increasing deviation from the parallel beam.

The implemented setup is shown in figure 6. A helium–neon laser at a wavelength of 632.8 nm was used for illumination. Non-polarizing beam splitter plates with split ratios of 50:50 were used for beam splitting. Due to the sharp drop in intensity in the



Figure 6: Mechanical setup for the proof of concept. (A) helium–neon laser at a wavelength of 632.8 nm, (B) beam splitter, (C) sample, (D) pinhole, (E) flat mirror, (F) flat mirror, (G) beamsplitter.

Table 2: Parameters of the components of the Mach–Zehnder interferometer design. The numbering corresponds to that shown in figure 5.

Component	Position (y, z) [mm]	Radius <sub>1</sub> [mm]	Conic <sub>1</sub> [mm]	Thickness [mm]	Radius <sub>2</sub> [mm]	Conic <sub>2</sub> [mm]	Material
Beamsplitter (b)	(0,20)	$\infty$	–	10	$\infty$	–	N–BK7
Flat mirror (c)	(50,30)	$\infty$	0	0	–	–	Silver
Beamexpander lens (d)	(50,40)	5	0	1	$\infty$	0	N–BK7
Beamexpander lens (e)	(50,190)	97.75	0	–	$\infty$	0	N–BK7
Beamcompressor lens (f)	(0,44)	97.75	0	5	$\infty$	0	N–BK7
Beamcompressor lens (g)	(0,237)	1	0	–	$\infty$	0	N–BK7
Sample (h)	(0,250)	$\infty$	–	1	$\infty$	–	scattering surfaces
Pinhole (i)	(0.9,260)	–	–	0	$\infty$	–	N–BK7
Collimator lens (j)	(0.9,300)	–36.549	–7.721	15	–18.79	–0.607	N–BK7
Beamsplitter (k)	(50,325)	$\infty$	–	10	$\infty$	–	N–BK7
flat mirror (m)	(10,340)	$\infty$	0	0	–	–	Silver

sample arm, a split ratio of 90:10 would have been more suitable, with the 90% being localized in the sample arm. The new split ratio will additionally improve the contrast in the interference pattern.

A thin preparation of artificially grown cells was used as sample. The used sample consisted of skeletal muscle–like constructs. The tissue was grown from myoblasts that were embedded in a fibrin hydrogel and mechanically stimulated in a bioreactor (Heher et al., 2015). Due to the small thickness of the preparation, multiple scattering with significantly different optical paths could be practically excluded. With the selected setup no A–Scan could be realized. However, the structure made it easier to generate an interference pattern.

### 3 RESULTS

#### 3.1 Numerical Simulation

The numerical simulation was carried out in accordance with the illustration from figure 5 in OpticStudio (ZEMAX LLC, 2020). The most important optical properties of the used components are listed in table 2. N–BK7 was used for all transmissive optical components. In practice, different materials may be used.

Beam expander and beam compressor were designed manually. In the final setup, these will be replaced by commercial beam expander systems. In the simulation the selection of the different scan depths takes place by using two scatter points located at a distance of one millimeter from one another. In a practically implemented setup, the interference patterns of

the scattering points of different depths (A–Scan) are possibly recorded sequentially by a movable pinhole in the sample arm in front of the beam splitter cube (k) in figure 5. This is not necessary in the simulation because the generated interference patterns are located sufficiently distant from one another.

The corresponding simulated interference patterns are shown in figure 7. Two sharply separated ring patterns of the two scattering points, situated at different depths, can clearly be seen.

The simulation basically demonstrates that the theoretical setup is suitable for reconstructing an A–Scan from the recorded interference patterns. It should be noted that the interference patterns will overlap in practice. A separation can be achieved via a pinhole in the sample arm in front of the beam splitting cube (k). In order to accelerate the A–scan, a line of pinhole diaphragms is recommended, which generates separate interference patterns from differ-

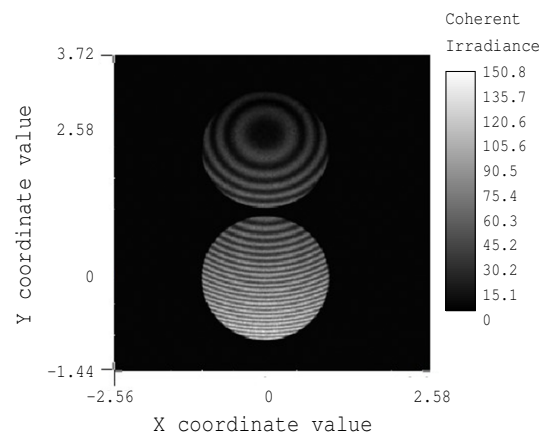


Figure 7: Simulation of the generated interference patterns for two different depths 1 mm apart in the sample.

ent sample depths, but which are relatively far apart. By moving the pinhole line over the distance between two holes, the entire scan is obtained in the time  $T/m$ , where  $T$  is the duration for a scan with shifting one pinhole and  $m$  is the number of used pinholes.

Due to the different optical paths, the two interference patterns are different, as expected. The center of the interference pattern is shifted, so that the center of the ring-shaped interference pattern in the upper image of the figure 7 lies in the center of the sensor, while the center of the ring-shaped interference pattern is shifted upwards for the second depth, shown in the lower image of figure 7. Using a larger sensor allows the center points of the interference patterns to remain searchable, which is necessary for the interpretation of the A-scan.

Basically, the simulation proves that the scattering from both tissue depths leads to an angular spectrum of the exiting rays which can be converted into parallel rays by means of the lens (j). The distance between the rays corresponds to the scan depth, starting with the point of entry of the light ray into the tissue up to a maximum scanning depth, which is limited on the one hand by the total internal reflection occurring at the exit surface and on the other hand by the NA of the lens (j) used. Both effects could be minimized in practice by using a contact gel between the tissue (h) and the pinhole (i) and a field lens that is positioned in the pinhole.

### 3.2 Experimental Proof of Concept

In order to provide the proof of concept in a simplified experimental version, all components for the realization of an A-scan were removed from the setup. The setup as shown in figures 4 and 6 was realized. Therefore, a simplified design as shown in figure 4 was used. The implemented setup is shown in figure 6.

In order to minimize the absorption of the light beam in the sample, a thin preparation should be used. More precisely, tissue with low absorption should be chosen. Artificially grown skeletal muscle cells in a thin-layer preparation were therefore used as a sample. These show a significant forward scatter.

Since no lens was used in the setup to parallelize the scattered rays, only small scattering angles could be detected, which are scattered almost parallel to the illumination light beam. At the same time, it had to be guaranteed that the illuminating beam would be absorbed as completely as possible. Since the waist of the illumination beam is approximately 0.5 mm, the pinhole behind the sample was shifted by 1 mm compared to the illumination beam. This guarantees that,

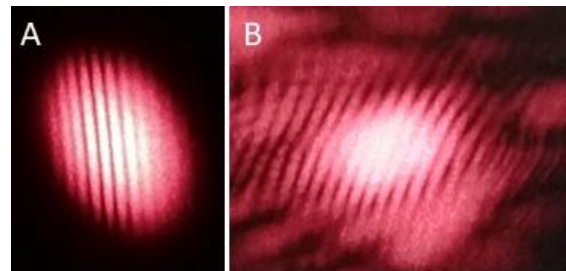


Figure 8: Measurement of the generated interference patterns for non-scattered light (A) and light scattered at a muscle cell sample (B).

on the one hand, only scattered rays can pass through the aperture, but the illuminating beam is absorbed and, on the other hand, the transmitted light has only a small angle with respect to the illuminating beam. This deviation in parallelism should be reflected in a distorted interference pattern.

With the simplified setup, the interference pattern shown in figure 8 was recorded. Figure 8 (A) shows the undistorted interference pattern generated at the output of a Mach-Zehnder interferometer. The setup did not contain a test sample or a pinhole, so that the interference pattern corresponds to that of an undisturbed Mach-Zehnder interferometer.

Figure 8 (B) shows the generated interference pattern after adding the test sample and the offset pinhole. The distortion in the interference pattern can be seen as a deformed envelope. However, the interference fringes can also be clearly detected in the simplified setup. The location of the scattering cannot be exactly determined due to the small thickness of the preparation and the lack of a lens for separating the various rays of the A-scan.

Since this setup is a pure proof of concept, no further measurement of the interference pattern was carried out. The setup proved to be very sensitive to vibrations. In addition, the relatively low intensity of the illumination laser used proved to be limiting.

## 4 DISCUSSION

The relatively shallow scan depth is the greatest limiting factor in optical coherence tomography. OCT can be used to create both laterally and in depth high resolution, three-dimensional scans of tissue, without the use of ionizing radiation. The achievable scan depth is limited by the usable light source intensity, the wavelength and the type of tissue to be scanned.

In order to reduce this limiting factor, but at the same time provide the advantageous properties of the OCT, in particular the independence from the scanned

tissue and the high, achievable resolution, a transmission version of the OCT was designed.

The Michelson interferometer usually used in classical OCT, with which backscattered light is analyzed interferometrically, is replaced by a Mach-Zehnder interferometer in which forward scattered light is to be analyzed.

In order to generate interference patterns with a sufficiently high contrast, some approximations must be fulfilled. On the one hand, the once scattered rays of the sample beam must be dominant over the multiple scattered rays. The setup in use also assumes that the examined tissue can be approximated as a plane-parallel plate.

The approximation that only single scattering can be measured limits the achievable result, since for multiple scattered light the formula 1 is no longer valid. Multiple scattering would result in the wrong depth of the scattering point, so that a clear assignment of the scattering point is no longer possible. This would manifest itself in a decrease in the contrast in the generated interference image. With a sufficiently large scattering angle, however, as can be seen in figure 2, it can be assumed that the amplitude of the multiple scattered light drops sufficiently quickly so that the reduction in the achievable contrast still allows the result to be clearly interpreted.

In a numerical simulation it was shown that the proposed setup is suitable for generating interference from rays that are scattered at different depths of the tissue. In addition, the proof of concept was provided that the proposed design for carrying out an A-scan works in principle. However, the tissue cannot be scanned in full depth, since, above a certain depth, scattered rays are totally reflected on the exit surface. In addition, the NA of the A-Scan-lens limits the measurable range of the representable scattered rays.

In a simplified experimental setup, the proof of concept was achieved and demonstrated that interference patterns can be generated with scattered rays in transmission in a Mach-Zehnder interferometer. Therefore this method is in principle able to function as the core of a tOCT.

## 5 CONCLUSION & FURTHER CHALLENGES

Possibilities for optimization were identified in both the numerical and the experimental setup.

The scan depth is limited by the total reflection occurring and by the NA of the A-scan lens. The former can be reduced by using a contact gel, similar to ultrasound, and the latter appears to be reducible by

using a field lens in the position of the pinhole. In addition, a numerical analysis should be carried out with more realistic dissemination models for tissue obtained from laboratory experiments. The Gaussian model used in the current simulation may not reflect reality adequately.

The influence of different split ratios of the beam splitter should be examined and optimized numerically and there is still no tolerance analysis of the components used.

In the next step, a tOCT including a complete A-scan will be implemented experimentally. In this setup it is to be examined how the A-scan can be implemented in practical application. The possible choice of a second pinhole in front of the beam splitter (k) from figure 5 and the scanning speed will depend on this.

Furthermore, it has to be analyzed in experimental investigations whether the back-calculation is also possible from the generated interference patterns for the illuminated structure. This analysis will be based on measurements of scattered light on tissue samples.

The maximum depth of penetration will depend on the wavelength used, the intensity of the light used and the tissue being screened. These examinations are to be carried out in the future.

In addition, the usability of different light sources, especially with regard to the desired wavelength used, should be investigated. Multi-wavelength scans could significantly improve the resolution of the scans generated.

## REFERENCES

- Bhandari, A., Hamre, B., Frette, O., Stamnes, K., and Stamnes, J. J. (2011). Modeling optical properties of human skin using mie theory for particles with different size distributions and refractive indices. *Optics Express*, 19(15):14549–14567. <https://doi.org/10.1364/OE.19.014549>.
- Bohren, Craig F. and Huffman, Donald R. (1983). *Absorption and Scattering of Light by Small Particles*. John Wiley & Sons, Inc, Clearance Center, 222 Rosewood Drive, Danvers, MA 01923.
- Born, M. and Wolf, E. (2005). *Principles in Optics*. Pergamon Press LTD., Headington Hill Hall, Oxford 4 & 5 Fitzroy Square, London W.1., Great Britain, 7<sup>th</sup> edition.
- Brezinski, Mark E. (2006). *Optical Coherence Tomography – Principles and Applications*. Elsevier Inc., 84 Theobald's Road, London WC1X 8RR, UK.
- Bushberg, Jerold T., Seibert, J. A., Leidholdt, Edwin M., and Boone, John M., editors (2012). *The Essential Physics of Medical Imaging*. Lippincott Williams & Wilkins, a Wolters Kluwer business, Two Commerce

- Square, 2001 Market Street, Philadelphia, PA 19103 USA, 3<sup>rd</sup> edition.
- Dance, David R., Christofides, S., Maidment, A. D. A., Mclean, I. D., and Ng, K. H., editors (2014). *Diagnostic Radiology Physics: A Handbook for Teachers and Students*. International Atomic Energy Agency, Vienna international Centre. Po box 100. 1400 Vienna, Austria.
- Demtröder, W. (2009). *Experimentalphysik – Band 2: Elektrizität und Optik*. Springer-Verlag Berlin Heidelberg, 5<sup>th</sup> edition.
- Drexler, W. and Fujimoto, James G., editors (2015). *Optical Coherence Tomography – Technology and Applications*. Springer Cham Heidelberg New York Dordrecht London, 2<sup>nd</sup> edition.
- Fercher, A. F., Drexler, W., Hitzberger, Christoph K., and Lasser, T. (2003a). Optical coherence tomography – principles and applications. *Rep Prog Phys*, 66:239–303. <https://doi.org/10.1088/0034-4885/66/2/2F204>.
- Fercher, A. F., Drexler, W., Hitzberger, Christoph K., and Lasser, T. (2003b). Optical coherence tomography – principles and applications. *Rep Prog Phys*, 66(2):239–303. <https://doi.org/10.1088/0034-4885/66/2/204>.
- Fujimoto, J. and Swanson, E. (2016). The development, commercialization, and impact of optical coherence tomography. *IOVS, Special Issue*, 57(9). <https://www.readcube.com/articles/10.1167/iovs.16-19963>.
- Guggenheim, Emily J., Lynch, I., and Rappoport, Joshua Z. (2017). Imaging in focus: Reflected light imaging: Techniques and applications. *Int J Biochem Cell Biol*, 83:65–70. <https://doi.org/10.1016/j.biocel.2016.12.008>.
- Heher, P., Maleiner, B., Prüller, J., Teuschl, A. H., Kollmitzer, J., Monforte, X., Wolbank, S., Redl, H., Rünzler, D., and Fuchs, C. (2015). A novel bioreactor for the generation of highly aligned 3d skeletal muscle-like constructs through orientation of fibrin via application of static strain. *Acta Biomater*, 24:251–26. <https://doi.org/10.1016/j.actbio.2015.06.033>.
- Hoppert, M. (2003). *Microscopic Techniques in Biotechnology*. WILEY-VCH Verlag GmbH & Co. KGaA, Weinheim, Germany.
- Mie, G. (1908). Beiträge zur Optik trüber Medien, speziell kolloidaler Metallösungen. *Annalen der Physik*, 4(25):377–445. <https://doi.org/10.1002/andp.19083300302>.
- Rathod, K. S., Hamshere, S. M., Jones, D. A., and Mathur, A. (2015). Intravascular ultrasound versus optical coherence tomography for coronary artery imaging – apples and oranges? *Interv Cardiol*, 10(1). <https://doi.org/10.15420/icr.2015.10.1.8>.
- Samei, E. and Peck, Donald J., editors (2019). *Hendee's Physics of Medical Imaging*. JohnWiley & Sons, Inc., 9600 Garsington Road, Oxford, OX4 2DQ, UK, 5<sup>th</sup> edition.
- Schützenberger, K., Pfister, M., Messner, A., Fröhlich, V., Garhöfer, G., Hohenadl, C., Schmetterer, L., and Werkmeister, R. M. (2019). Comparison of optical coherence tomography and high frequency ultrasound imaging in mice for the assessment of skin morphology and intradermal volumes. *Scientific Reports*, 9(13643). <https://doi.org/10.1038/s41598-019-50104-4>.
- Vo-Dinh, T., editor (2003). *Biomedical Photonics Handbook*. CRC Press LLC, 2000 N.W. Corporate Blvd., Boca Raton, Florida 33431, USA, 1<sup>st</sup> edition.
- Webster, John G., Ritenour, E., Tabakov, S., and Ng, K., editors (2000). *Webb's Physics of Medical Imaging*. CRC Press Taylor & Francis Group, 6000 Broken Sound Parkway NW, Suite 300, USA, 2<sup>nd</sup> edition.
- ZEMAX LLC (2020). Opticstudio®. <https://www.zemax.com/products/opticstudio>.